Article

Cobalt−Nickel Layered Double Hydroxides on Electrospun MXene for Superior Asymmetric Supercapacitor Electrodes

Hao Jiang, Jinbing Cheng,* Junbao He, Chunying Pu, Xiaoyu Huang, Yichong Chen, Xiaohong Lu, Yang Lu, Deyang Zhang, Zhaorui Wang, Yumin Leng,* Paul K. Chu, and Yongsong Luo*
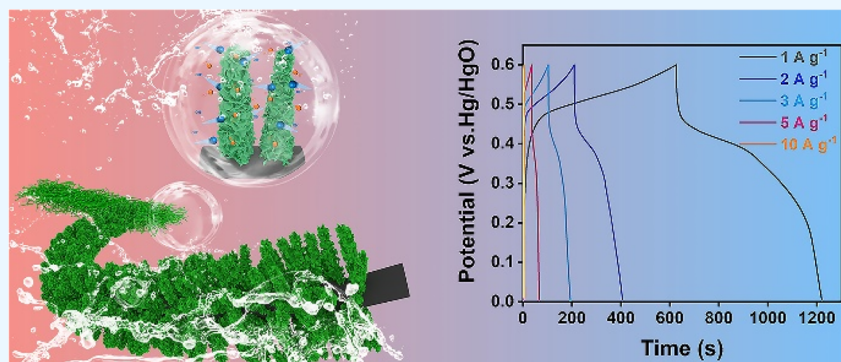
Read Online

ACCESS | Metrics & More | Article Recommendations | Supporting Information

ABSTRACT: Flexible electrodes for energy storage and conversion require a micro-nanomorphology and stable structure. Herein, MXene fibers (MX-CNF) are fabricated by electrospinning, and Co-MOF nanoarrays are prepared on the fibers to form Co-MOF@ MX-CNF. Hydrolysis and etching of Co-MOF@MX-CNF in the Ni^{2+} solution produce cobalt−nickel layered double hydroxide (CoNi-LDH). The CoNi-LDH nanoarrays on the MX-CNF substrate have a large specific surface area and abundant electrochemical active sites, thus ensuring effective exposure of the CoNi-LDH active materials to the electrolyte and efficient pseudocapacitive energy storage and fast reversible redox kinetics for enhanced charging−discharging characteristics. The CoNi-LDH@MX-CNF electrode exhibits a discharge capacity of 996 F g^{-1} at a current density of 1 A g^{-1} as well as 78.62% capacitance retention after 3,000 cycles at 10 A g^{-1}. The asymmetric supercapacitor (ASC) comprising the CoNi-LDH@MX-CNF positive electrode and negative activated carbon electrode shows an energy density of 48.4 Wh kg^{-1} at a power density of 499 W kg^{-1} and a capacity retention of 78.9% after 3,000 cycles at a current density of 10 A g^{-1}. Density-functional theory calculations reveal the charge density difference and partial density of states of CoNi-LDH@MX-CNF confirming the large potential of the CoNi-LDH@ MX-CNF electrode in energy storage applications.

1. INTRODUCTION

Sustainable energy storage devices have attracted widespread attention, and in particular, supercapacitors (SCs) are important due to their advantages in electrochemical energy storage, fast charging, good safety, high power density, and excellent cycling stability.[1−5] Layered double hydroxides (LDHs) with a unique size and structure, remarkable redox activity and anion exchange capability are desirable electrode materials for supercapacitors.[6−9] However, their poor conductivity, limited exposed surface area, and restacking hinder the complete utilization of the energy storage potential in electrochemical processes.[10−12] Modification and functionalization of layered double hydroxides (LDH) to maximize their electrochemical energy storage capabilities are being pursued, and the construction of special nanostructures can enhance the electrochemical properties of LDH materials.[13,14]

The two-dimensional layered metal carbide, titanium carbide also known as MXene (MX), is promising in electrochemical energy storage applications due to its hydrophilicity, high conductivity (∼15,000 S cm^{-1}), and good mechanical properties.[15−17] It has been employed to enhance the electrochemical performance of metal hydroxides. For example, Huang et al. have anchored the NiFe-LDH arrays on $Ti_3C_2T_x$-MXene sheets to improve the structural stability, conductivity, and redox kinetics.[18] Wang et al. have synthesized interlayered nanoscale LDH-MXene-LDH by a coprecipitation method to improve electron transfer and long-term cycling stability.[19] However, MXene tends to restack due
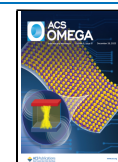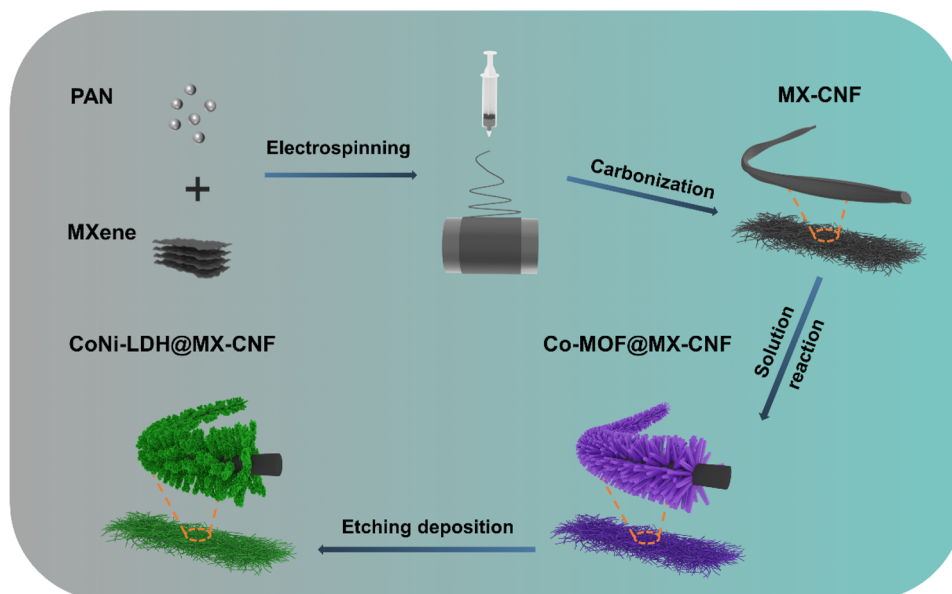
Figure 1. Schematic illustration illustrating the preparation of CoNi-LDH@MX-CNF.
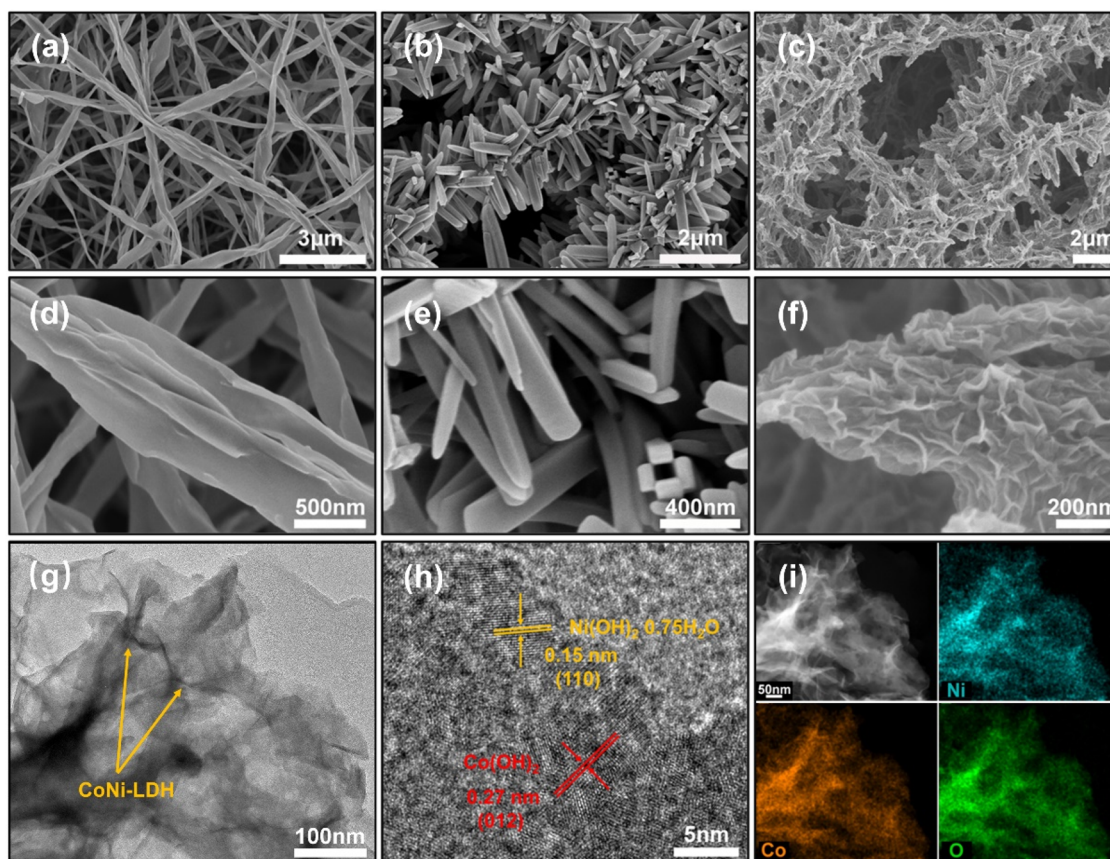

Figure 2. (a, d) SEM images of the MX-CNF, (b, e) SEM images of Co-MOF@MX-CNF, (c, f) SEM images of CoNi-LDH@MX-CNF, (g, h) TEM images of CoNi-LDH@MX-CNF, (i) TEM elemental maps.

to van der Waals forces between layers and is also prone to oxidation.[20,21] To address the issues of restacking and oxidation of MXene, various approaches have been proposed.[16] One technique is to combine MXene with carbonaceous materials such as carbon nanotubes and graphene;[22,23] another approach is to encapsulate MXene with fibers by electrostatic spinning. In fact, electrospinning is a simple, versatile, and cost-

effective method to produce nonwoven mats of nanofibers, allows good control of the fiber diameter, orientation, and other parameters, and is suitable for MXene.[24,25]

In this work, MXene is confined in carbon nanofibers by electrospinning to produce an MXene-carbon nanofiber composite (MX-CNF). In this flexible structure, self-stacking of MXene and oxidation is mitigated. MX-CNF is used as the
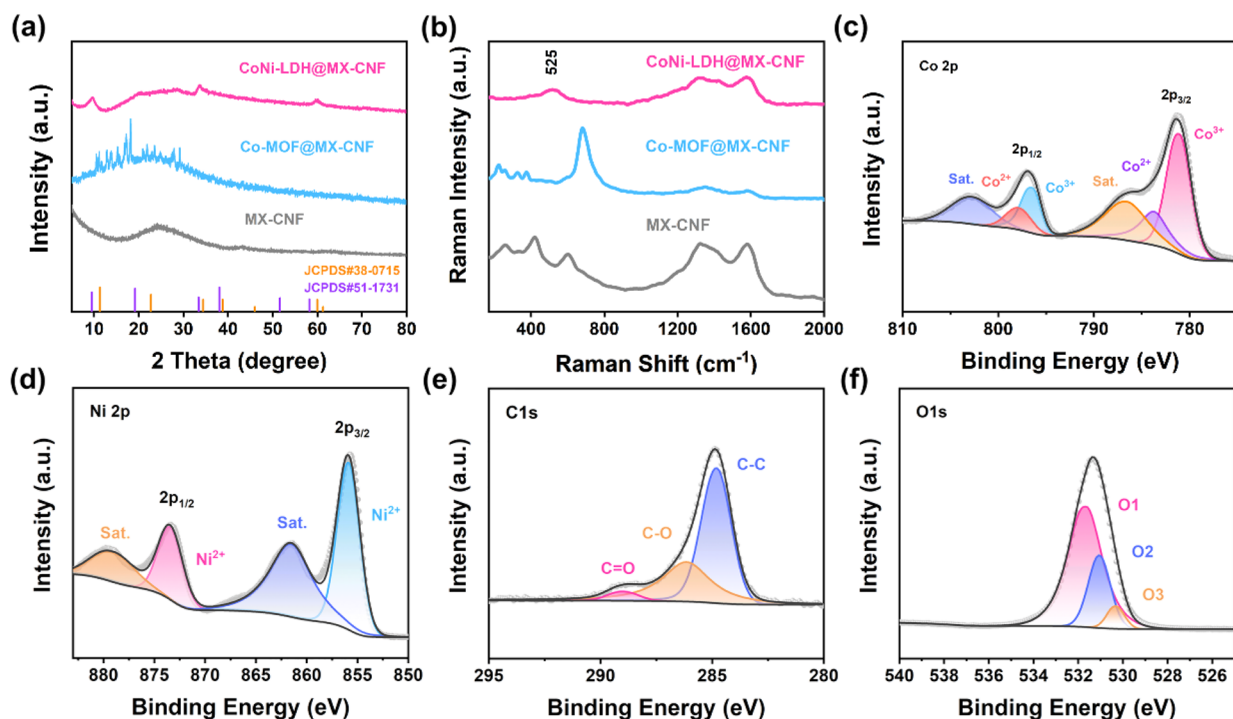
Figure 3. (a) XRD patterns of MX-CNF, Co-MOF@MX-CNF, and CoNi-LDH@MX-CNF, (b) Raman scattering spectra of MX-CNF Co-MOF@MX-CNF and CoNi-LDH@MX-CNF, (c) XPS Co 2p spectrum, (d) XPS Ni 2p spectrum, (e) XPS C 1s spectrum, and (f) XPS O 1s spectrum.

substrate to load CoNi-LDH to maximize the aggregation of CoNi-LDH nanoarrays, increase the exposed surface area for active sites, minimize reaggregation, and improve electrolyte penetration. The CoNi-LDH@MX-CNF electrode incorporated into an asymmetric supercapacitor shows excellent electrical conductivity and high specific capacitance, boding well for energy storage applications.

2. EXPERIMENTAL SECTION

Layered MXene flakes were synthesized through etching and exfoliation of the Ti$_3$AlC$_2$ MAX phase. Few-layered MXene flakes were combined with a solution of DMF and PAN to form a spinning solution, which was then electrospun and subjected to high-temperature carbonization to produce MX-CNF. The MX-CNF membrane was immersed in a mixed solution containing a specific ratio of dimethylimidazole and cobalt nitrate. Through the in situ growth of Co-MOF on the surface, Co-MOF@MX-CNF was obtained. The Co-MOF@MX-CNF membrane was subsequently immersed in a solution containing a certain amount of nickel sulfate for hydrolysis etching, resulting in the formation of CoNi-LDH@MX-CNF. For detailed information, please refer to the Supporting Information.

3. RESULTS AND DISCUSSION

The synthesis of CoNi-LDH@MX-CNF is illustrated in Figure 1. The PAN fiber film was prepared by adding MXene and PAN DMF liquid by electrospinning and then undergoes preoxidation and carbonization to obtain MX-CNF. The Ti$_3$AlC$_2$ MAX phase and etched MXene sheets are characterized. SEM is performed to examine the morphologies before and after etching (Figure S1a,b). Ti$_3$AlC$_2$ MAX has a multilayered structure, while the etched MXene has a few-layered structure. The X-ray diffraction (XRD) patterns in

Figure S2 reveal a difference between the pre-etched Ti$_3$AlC$_2$ MAX and postetched MXene.[26] A sharp and broad peak at 7° arising from the (002) plane is detected from the etched MXene, indicating a larger interlayer spacing and smaller layer thickness due to selective etching of Al in Ti$_3$AlC$_2$ MAX.[27] The disappearance of the (104) peak at 38.8° from Ti$_3$AlC$_2$ corroborates the etching of Al.[16] Subsequently, the MXene/ PAN electrospun membrane is preoxidized and carbonized to produce MX-CNF, and the straight shape of the preoxidized MXene/PAN nanofiber is maintained (Figure S3). In the preoxidation stage, the PAN/MX-CNF precursor undergoes cyclization reactions, resulting in the formation of pyridine-like structures and similar moieties. As carbonization progresses, these cyclized structures undergo dehydrogenation and begin to laterally connect, forming graphite-like structures, which further contribute to the shrinkage. As seen in Figure 2a, bent fibers are evident, and as demonstrated in Figure S3b,c, the carbonized MX-CNF experiences contraction.[28−30] To confirm the presence of MXene in the carbonized MX-CNF fibers, TEM images are acquired, and as shown in Figure S4, the high-magnification SEM image of the MX-CNF fibers shows the presence of MXene in Figure S4a. The TEM images of the MX-CNF fibers in Figure S4b,c indicate the existence of MXene in the fibers with a lattice spacing of 0.26 nm corresponding to the (100) plane of MXene.[31] The elemental maps obtained from MX-CNF reveal that the distributions of Ti, C, and N correspond to the locations of MXene in the fibers.

MX-CNF is used as a substrate to produce Co-MOF nanorod arrays by a simple room-temperature liquid reaction. The Co-MOF@MX-CNF intermediate is then immersed in a solution containing nickel sulfate for ion etching, deposition, and growth by hydrolysis. In this process, Ni^{2+} undergoes weak hydrolysis in nearly neutral aqueous solution to form a small
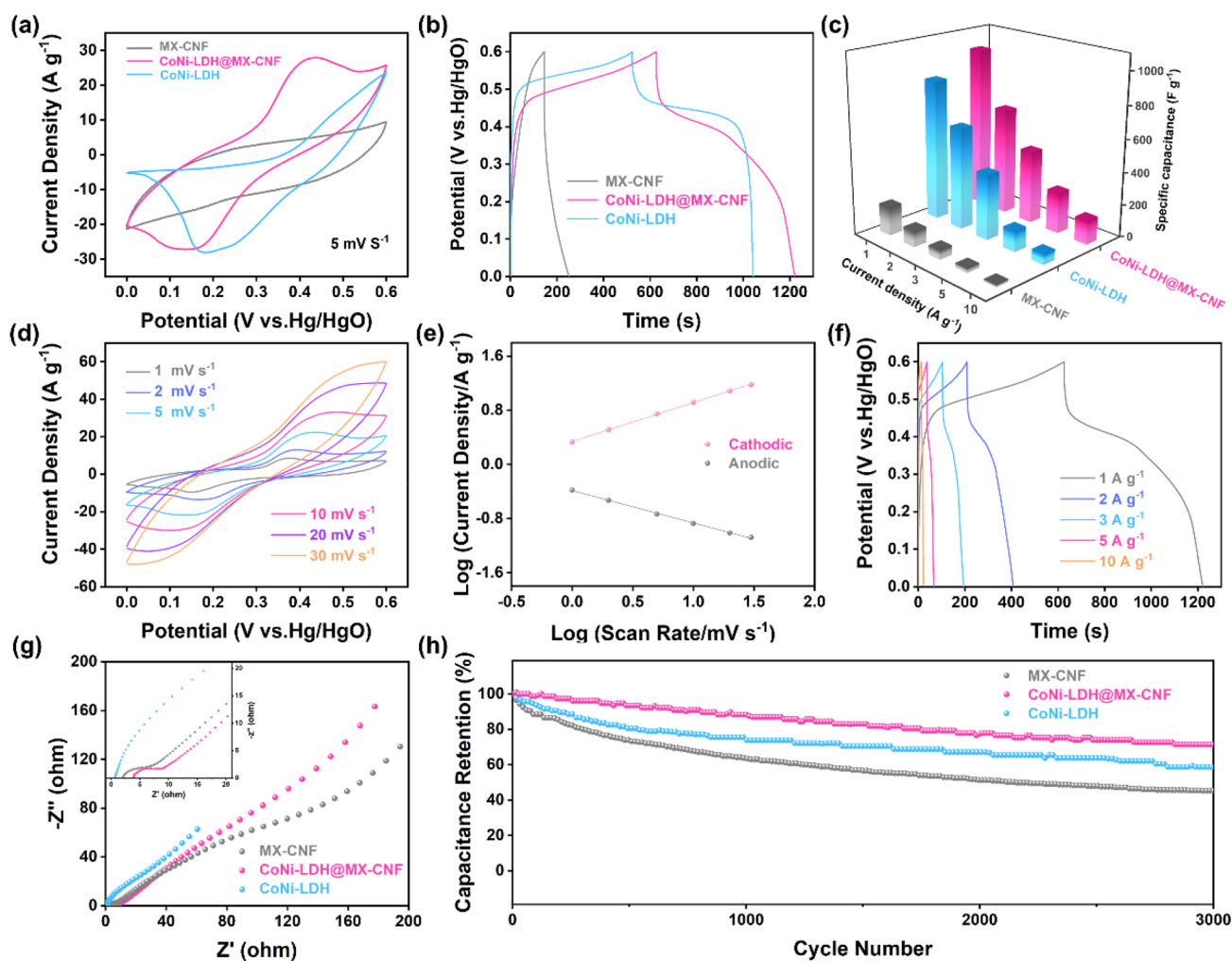
Figure 4. (a) CV spectra acquired at a scanning rate of 5 mV s^{-1}, (b) galvanostatic discharging/charging curves obtained at 1 A g^{-1}, (c) specific capacitances of the electrodes at different current densities, (d) CV curves of CoNi-LDH@MX-CNF at different scanning rates, (e) corresponding *b* values of the cathodic and anodic peaks of the as-prepared CoNi-LDH@MX-CNF, (f) GCD curves of CoNi-LDH@MX-CNF for different densities, (g) Nyquist plot of CoNi-LDH@MX-CNF and equivalent circuit, and (h) cycling stability of CoNi-LDH@MX-CNF at 10 A g^{-1}.

amount of nickel hydroxide and H$^+$. The 2-MIM ligand in Co-MOF captures H$^+$ to form soluble 2-MIM H$^+$ that dissolve in the solution leading to the release of Co^{2+}. Similar to Ni^{2+}, the released Co^{2+} undergoes hydrolysis to form Co(OH)$_2$ and H$^+$, which completes with the exchange between hydroxide and 2-MIM ligands in Co-MOF.[1] As the exchange consumes the 2-MIM ligands and H$^+$, Ni^{2+} and Co^{2+} are further hydrolyzed to produce more Co(OH)$_2$ and Ni(OH)$_2$, which are deposited on the surface of the rod-shaped Co-MOF framework to form a sheet-like CoNi-LDH structure.[32] The SEM images in Figure 2a,d show the MX-CNF membrane and encapsulation of MXene sheets in the carbon fibers, which enhances the flexibility, conductivity, and hydrophilicity of the spun membrane.[33] The surface contact angles are shown in Figure S5. The contact angle on the CNF membrane is 26.7° (Figure S5b), but that on MX-CNF is significantly smaller (9.83°) as shown in Figure S5a, indicating improved wetting. To confirm the mechanical flexibility, bending tests are performed as shown in Figure S6.

X-ray diffraction (XRD) patterns are acquired from MX-CNF. The broad peak at 23° corresponds to carbon, but no titanium dioxide peak is detected, indicating decreased MXene oxidation rendered by the carbon layer. The Raman scattering

spectra of MX-CNF in Figure 3b exhibit three peaks from MXene at 258 cm^{-1}, 424 cm^{-1}, and 603 cm^{-1} after carbonization at 800 °C.[34] In contrast, no additional peaks are observed from the carbon nanofibers (CNF) without the addition of MXene, as shown in Figure S7. Synthesis of Co-MOF on MX-CNF is confirmed.[7] Compared with the precursor, CoNi-LDH@MX-CNF shows a different XRD pattern, indicating complete transformation by hydrolysis etching. The diffraction peaks can be indexed to Co(OH)$_2$ (JCPDS 51-1731) and Ni(OH)$_2$·0.75H$_2$O (JCPDS 38-0715). However, CoNi-LDH@MX-CNF shows the (003) plane of the layered nickel hydroxide phase that deviates by 11.3° from the standard position, as shown in Figure 3a. This shift to a lower position at 9.7° indicates a larger interlayer spacing in CoNi-LDH@MX-CNF. This is because nickel sulfate is the etching source, resulting in slower growth on the nanosheets during the in situ hydrolysis-induced exchange synthesis of the CoNi-LDH microstructure in a nickel sulfate solution.[1] Consequently, the generated nanosheets exhibit a more regular arrangement, and sulfate ions influence the formation of the cobalt hydroxide crystal phase. Acting as charge-balancing ions between the layers, sulfate ions also affect the interlayer spacing. A larger interlayer spacing accommodates more
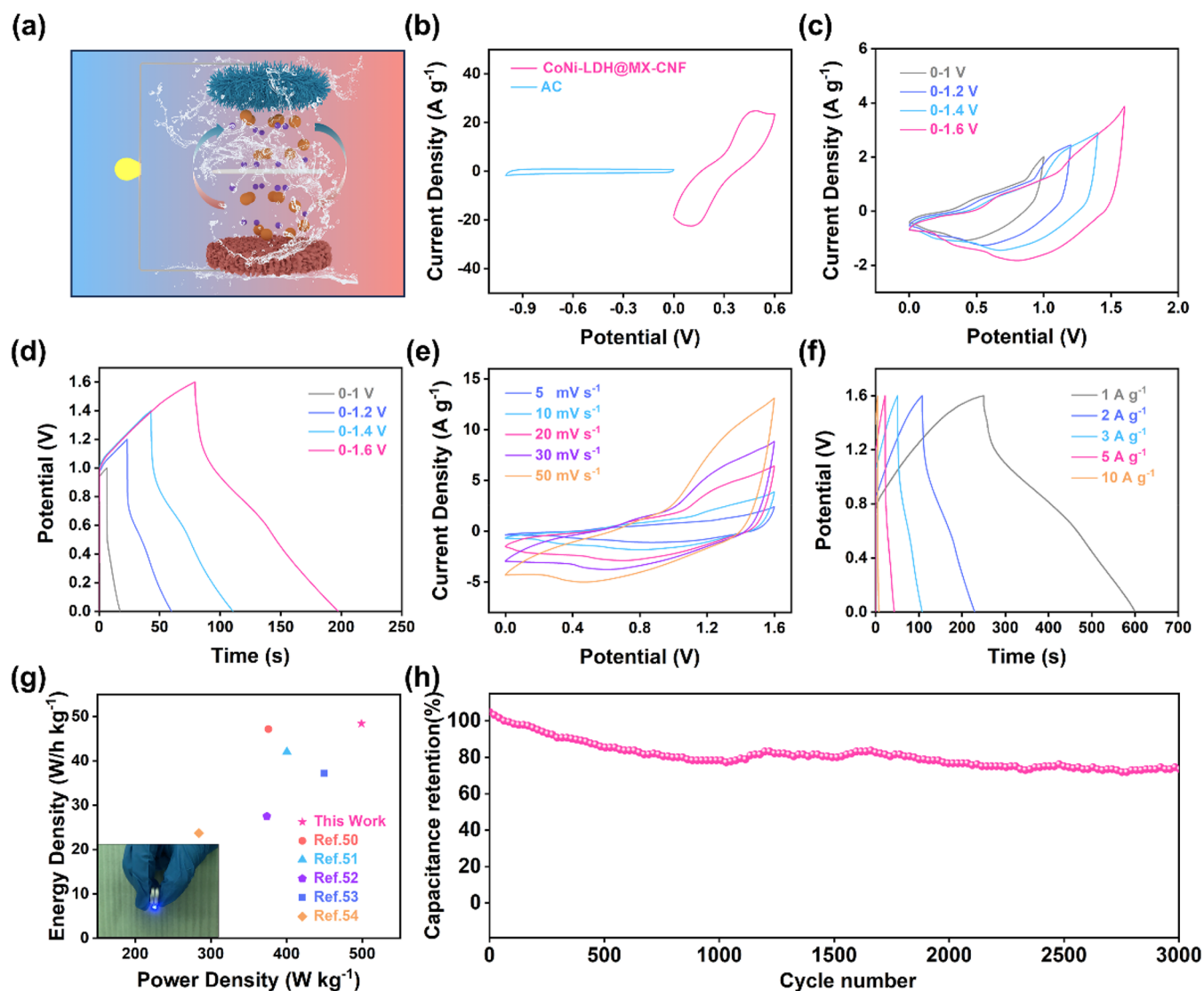
Figure 5. (a) Schematic of CoNi-LDH@MX-CNF//AC ASC, (b) CV curves of CoNi-LDH@MX-CNF and AC acquired from a three-electrode system at 10 mV s^{-1}, (c) CV curves of CoNi-LDH@MX-CNF//AC at 30 mV s^{-1} in voltage windows from 1.0 to 1.6 V, (d) GCD curves of CoNi-LDH@MX-CNF//AC at 10 A g^{-1} in voltage windows from 1.0 to 1.6 V, (e) CV curves of CoNi-LDH@MX-CNF//AC obtained at the different scanning rates, (f) GCD curves of CoNi-LDH@MX-CNF//AC at different densities, (g) Ragone plots (inset showing powering of LED), and (h) cycling stability of CoNi-LDH@MX-CNF//AC at 10 A g^{-1}.

electrolyte ions, particularly hydroxide ions, and allows them to access the active sites at the interlayer interfaces more easily to participate in the electrochemical redox reactions to boost the electrochemical activity.[35]

The SEM images of Co-MOF@MX-CNF are displayed in Figure 2b,e. The Co-MOF layers are dense and uniform on the surface of the MX-CNF fibers. Co-MOF has a smooth surface and uniform thickness and serves as the sacrificial template for the multilevel heterostructure of CoNi-LDH which is preserved throughout the reaction. The SEM images in Figure 2c,f demonstrate the formation of a well-defined three-dimensional structure composed of uniformly distributed rod-like Co-MOF frameworks and CoNi-LDH nanosheets on the surface. Figure 2g shows the formation of numerous ultrathin nanosheets consistent with SEM. The high-resolution TEM image in Figure 2h confirms the polycrystalline nature, displaying two distinct sets of stripes. The stripe with a *d*-spacing of 0.15 nm corresponds to the (110) plane of Ni(OH)$_2$·0.75H$_2$O (JCPDS 38-0715), while that with a

spacing of 0.27 nm matches the (012) plane of Co(OH)$_2$ (JCPDS 51-1731).[1,5,36] The elemental maps of CoNi-LDH@MX-CNF demonstrate uniform distributions of O, Co, and Ni corroborating uniform growth of CoNi-LDH micronanosheets on MX-CNF.

To further confirm the formation of CoNi-LDH, the Raman scattering spectra of Co-MOF@MX-CNF and CoNi-LDH@MX-CNF are shown in Figure 3b.[32] In addition to the peak at 258 cm^{-1} associated with MXene, new peaks have emerged at 219 cm^{-1}, 334 cm^{-1}, 380 cm^{-1}, and 683 cm^{-1} corresponding to the vibrational mode of the 2-methylimidazolate ligand and the Co−N bond.[37−41] This substantiates the successful synthesis of Co-MOF on MX-CNF. After the etching-deposition-growth process, the Raman peaks of the Co-MOF@MX-CNF precursor disappeared, and CoNi-LDH@MX-CNF exhibits a broad peak of the Ni-O/Co-O symmetric stretching mode at 525 cm^{-1}.[32,36] The characteristic peaks of the Co-MOF precursor are conspicuously absent in the Raman
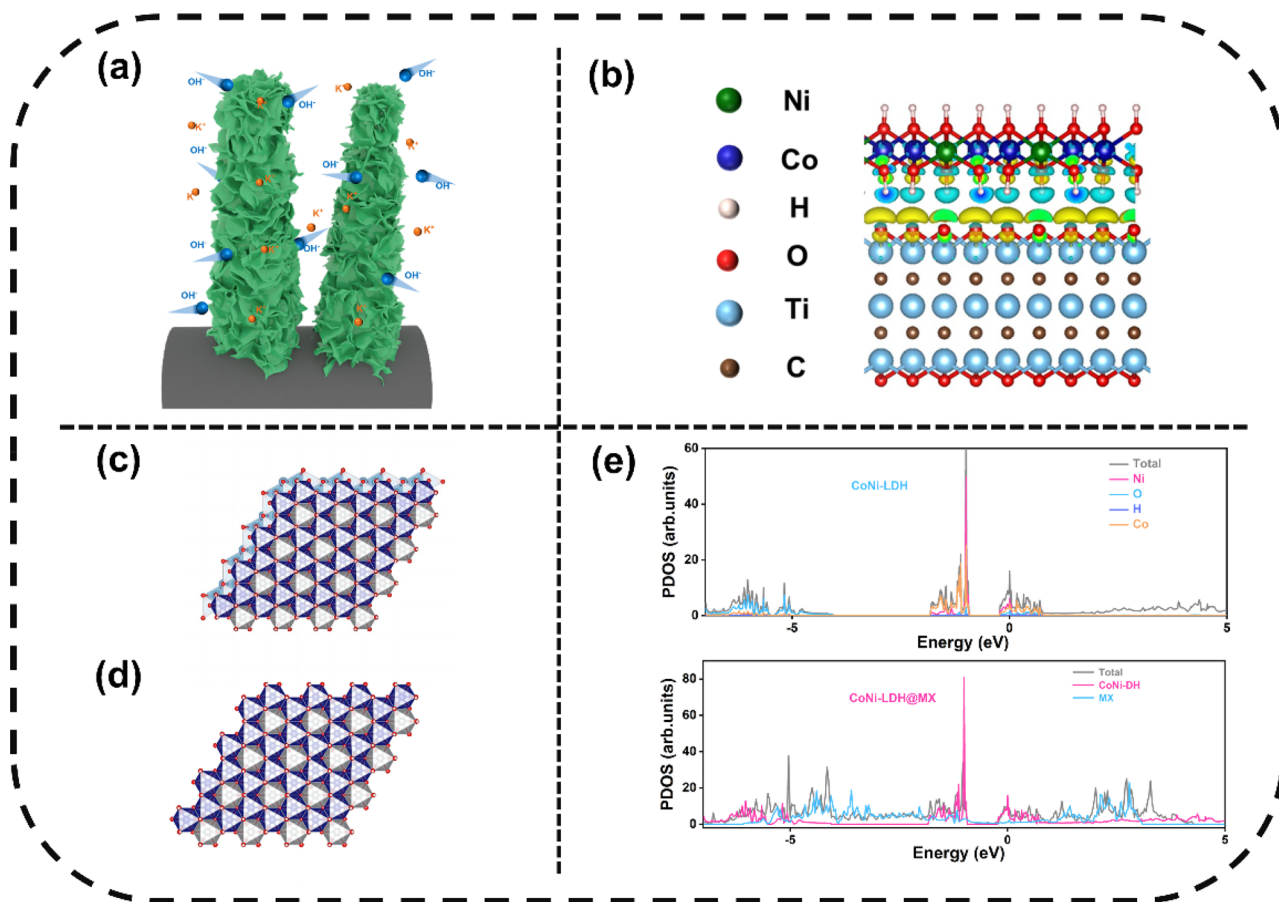
Figure 6. (a) Schematic diagram showing the electrochemical performance of CoNi-LDH@MX-CNF, (b) charge density difference of CoNi-LDH@MX-CNF, (c, d) schematic showing the relaxed structures of CoNi-LDH@MX-CNF and CoNi-LDH, and (e) calculated PDOSs of CoNi-LDH@MX-CNF and CoNi-LDH.

spectra of the resultant CoNi-LDH@MX-CNF, implying complete conversion of Co-MOF.

The chemical composition and chemical state of CoNi-LDH@MX-CNF are determined by X-ray photoelectron spectroscopy (XPS). Compared with MX-CNF (Figure S8b), the presence of Co and Ni in the etched CoNi-LDH@MX-CNF (Figure S8a) indicates the growth of CoNi-LDH on the fibers. In the Co 2p spectrum in Figure 3c, the peaks at 781.0 and 796.5 eV correspond to the $2p_{3/2}$ and $2p_{1/2}$ orbitals of Co^{3+}. The peaks at 797.8 and 783.8 eV are assigned to the Co $2p_{1/2}$ and $2p_{3/2}$ orbitals of Co^{2+},[42−44] and the other peaks are satellite peaks (denoted as "Sat."), indicating that the layered nanoscale array simultaneously contains both Co^{2+} and Co^{3+} respectively. The two peaks at 786.0 and 802.6 eV in the Ni 2p spectrum in Figure 3d are satellite peaks (denoted as "Sat."), and the two spin−orbit peaks of Ni $2p_{3/2}$ and $2p_{1/2}$ are located at 855.8 and 873.4 eV, respectively.[45,46] The two satellite peaks (denoted as "Sat.") are located at 861.54 and 879.03 eV. Figure 3e shows the C 1s spectrum and the peaks at 284.8, 286.2, and 289.0 eV correspond to C−C, C−O, and C=O.[47] Figure 3f shows the O 1s spectrum, and the peaks at 531.6, 531, and 530.4 eV correspond to C−O, C=O, and M−O (M = Ni, Co).[47]

4. ELECTROCHEMICAL PROPERTIES

CoNi-LDH@MX-CNF is evaluated by cyclic voltammetry (CV) using a three-electrode system in which the working electrode is CoNi-LDH@MX-CNF, the reference electrode is Hg/HgO, a platinum foil electrode was employed as the counter electrode, and 3 M potassium hydroxide is the electrolyte. The scanning rate is 5 mV s^{-1}. The CoNi-LDH was similarly tested by applying it to a nickel mesh. As shown in Figure 4a, the redox peaks of CoNi-LDH@MX-CNF represent the Faradaic redox reactions involving Ni^{3+}/Ni^{2+} and Co^{3+}/Co^{2+}.[48] The CoNi-LDH@MX-CNF electrode shows a larger CV area indicating superior electrochemical activity compared to CoNi-LDH (Figure S9a).[49] Figure 4b compares the charging and discharging time at a current density of 1 A g^{-1} between CoNi-LDH@MX-CNF and the other electrodes. CoNi-LDH@MX-CNF showed a longer discharging time and higher capacity. The prominent redox peaks of CoNi-LDH@MX-CNF at different scanning rates (1−30 mV s^{-1}) are presented in Figure 4d. The discharging rates of CoNi-LDH@MX-CNF at 1, 2, 3, 5, and 10 A g^{-1} are 996, 659, 450, 254, and 150 F g^{-1} respectively, all of which are higher than those of CoNi-LDH (Figure S9c) and MX-CNF (Figure S9d) under the same conditions (Figure 4c). The outcome highlights the superior electrochemical properties of the CoNi-LDH@MX-CNF composite structure. Figure 4d presents the CV curves of the CoNi-LDH@MX-CNF electrode at different scanning rates of 1−30 mV s^{-1}, and the redox peaks represent the Faradaic redox reactions of Co and Ni ions. According to the cathodic and anodic peak potentials in Figure 4e, the b values are 0.574 and 0.477, respectively, indicating both the intrinsic diffusion charge storage characteristics and external capacitive behavior. The GCD curves of the CoNi-LDH@MX-CNF

electrode at different current densities are presented in Figure 4f, which shows the typical pseudocapacitive behavior. Figure 4g presents the Nyquist plots of CoNi-LDH@MX-CNF, CoNi-LDH, and MX-CNF. In the low-frequency region, compared to the MX-CNF electrode, CoNi-LDH@MX-CNF has steeper slopes indicative of smaller diffusion resistance. At a current density of 10 A g^{-1}, the capacitance retention rates of the three materials are determined after 3,000 cycles. The CoNi-LDH@MX-CNF electrode shows a capacitance retention of 78.62%, whereas CoNi-LDH and MX-CNF electrodes show only 65.43% and 45.27%, respectively. The electrode after cycling is examined, and Figure S10 discloses insignificant alteration after cycling confirming the good stability.

To evaluate the practical feasibility of the electrode, an asymmetric supercapacitor (ASC) is assembled, as shown in Figure 5a with CoNi-LDH@MX-CNF as the positive electrode, activated carbon (AC) as the negative electrode, and 3 M potassium hydroxide as the electrolyte. CV is performed on the CoNi-LDH@MX-CNF and AC electrodes (Figure S11) separately in a three-electrode system with 3 M potassium hydroxide as the electrolyte at a scanning rate of 10 mV s^{-1}. The stable voltage range of CoNi-LDH@MX-CNF and AC are determined to be 0−0.6 and −1−0 V, respectively. Figure 5c shows the CV curves of the ASC in different voltage windows, and the stable operating voltage can be extended to 1.6 V. Figure 5d shows the GCD curves of the ASC in different voltage ranges at a current density of 2 A g^{-1}, and the ASC is stable at 1.6 V.

The properties of the ASC are then evaluated using a two-electrode system in the voltage window of 0−1.6 V. Figure 5e presents the CV curves of the ASC, and Figure 5b shows the CV curves of the CoNi-LDH@MX-CNF//AC ASC at different scanning rates from 5 mV s^{-1} to 50 mV s^{-1}. With increasing scanning rates, no significant distortion is observed from the CV curves, demonstrating stable capacitive behavior. Figure 5f shows the GCD curves of the CoNi-LDH@MX-CNF//AC ASC at current densities from 1 A g^{-1} to 10 A g^{-1}. The GCD curves maintain good symmetry at different current densities, suggesting electric double-layer capacitance and excellent electrochemical reversibility. Figure 5g shows the Ragone plot of the CoNi-LDH@MX-CNF//AC ASC for the energy and power density. At a power density of 499 W kg^{-1}, the energy density is 48.4 Wh kg^{-1}. The values of CoNi-LDH@MX-CNF//AC ASC are much higher than those of previously reported LDH systems including Co$_3$O$_4$@NiMn-LDH/Ni//AC,[50] CoNiLDH-350P@CFC//AC,[51] NiCo-LDH//AC,[52] NiP@CoAl-LDH//AC,[53] and Ni$_x$Co$_{1-x}$-LDH-ZTO//AC.[54] To evaluate the practical performance of the CoNi-LDH@MX-CNF//AC ASC, two ASCs are connected in series to power a blue LED in the voltage range 0−3 V. Figure 5h shows the long-term cycling characteristics of the CoNi-LDH@MX-CNF//AC ASC at a current density of 1 × 10 A g^{-1}. After 3,000 cycles, the CoNi-LDH@MX-CNF//AC ASC retains 78.9% of the initial capacity confirming the excellent cycling stability and application potential.

The improvement in the electrochemical characteristics of the CoNi-LDH@MX-CNF electrode is mainly attributed to the vertical anisotropic nanoarray structure, which effectively increases the number of active sites of CoNi-LDH in contact with ions in the solution. Direct growth of the nanoarrays on the surface reduces the interfacial resistance between the conductive substrate and active materials consequently providing electronic paths to improve ion/electron transfer while preserving the structure of the materials, as shown in Figure 6a. By analysis of the storage characteristics and performing first-principles calculations, the charge density difference and partial density of states (PDOS) of CoNi-LDH@MX-CNF are analyzed. Figure 6b shows that electrons are transferred from the hydroxide of LDH to the top oxygen atoms of MXene at the interface between the CoNi-LDH and MX-CNF layers. The charge transfer confirms the strong chemical bond between MXene and CoNi-LDH and supports the formation of electron transfer channels perpendicular to each layer to enhance the electron transfer at the CoNi-LDH@MX-CNF interface. The heterojunction in CoNi-LDH@MX-CNF is simplified to a monolayer of CoNi-LDH (Ni:Co = 1:1) on the MXene carrier in Figure 6c,d. Figure 6e shows that the synergistic electronic interaction of CoNi-LDH@MX-CNF is enhanced compared to that of pure CoNi-LDH on account of the fast electron transfer in the CoNi-LDH@MX-CNF system. In fact, the electronic states around the Fermi energy level are continuous and exhibit metallic properties.

5. CONCLUSIONS

MXene-spun nanofibers (MX-CNF) are used as the substrate for *in situ* liquid-phase growth of Co-MOF. Ni^{2+} hydrolysis is performed for etching and deposition in the fabrication of CoNi-LDH nanoarrays. CoNi-LDH@MX-CNF has a dense distribution of CoNi-LDH nanoarrays on the fibers, a large specific surface area, and abundant active sites to facilitate rapid diffusion of electrolyte ions and enhance the kinetics of the redox reactions. At 1 A g^{-1}, the electrode exhibits a specific capacitance of 996 F g^{-1} and capacity retention of 78.62% after 3,000 cycles. The asymmetric supercapacitor (ASC) consisting of CoNi-LDH@MX-CNF as the positive electrode and activated carbon as the negative electrode shows a high energy density of 48.4 Wh kg^{-1} at a power density of 499 W kg^{-1}. It can power an LED in the voltage range of 0−3 V. After cycling 3,000 times at a current density of 10 A g^{-1}, the device retains 78.9% of the initial capacity, thus demonstrating excellent cycling stability and practical potential in supercapacitors.

■ ASSOCIATED CONTENT

ⓈI Supporting Information

The Supporting Information is available free of charge at https://pubs.acs.org/doi/10.1021/acsomega.3c06674.

Synthesis of MXene, MX-CNF, Co-MOF@MX-CNF, CoNi-LDH@MX-CNF; SEM of Ti$_3$AlC$_2$, MXene, Co-MOF, and CoNi-LDH; XRD patterns of Ti$_3$AlC$_2$ and MXene; SEM image of the MXene/PAN nanofiber; TEM and TEM elemental maps of MX-CNF; contact angles of MX-CNF and CNF; MX-CNF bending test picture; Raman scattering spectrum of CNF; XPS survey spectra of CoNi-LDH@MX-CNF and MX-CNF; CV and GCD of CoNi-LDH and MX-CNF electrode; SEM of CoNi-LDH@MX-CNF electrode after cycles; CV and GCD of AC electrode (PDF)

■ AUTHOR INFORMATION

Corresponding Authors

Jinbing Cheng − *Henan International Joint Laboratory of MXene Materials Microstructure, College of Physics and Electronic Engineering, Nanyang Normal University, Nanyang 473061, P. R. China*; Email: chengjinbing1988@163.com

Yumin Leng − *School of Mathematics and Physics, Anqing Normal University, Anqing 246133, P. R. China*; Email: yumin_leng@126.com

Yongsong Luo − *Henan International Joint Laboratory of MXene Materials Microstructure, College of Physics and Electronic Engineering, Nanyang Normal University, Nanyang 473061, P. R. China; Key Laboratory of Microelectronics and Energy of Henan Province, Engineering Research Center for MXene Energy Storage Materials of Henan Province, Henan Joint International Research Laboratory of New Energy Storage Technology, Xinyang Normal University, Xinyang 464000, P. R. China;* orcid.org/0000-0002-8000-3126; Email: ysluo@xynu.edu.cn

Authors

Hao Jiang − *Henan International Joint Laboratory of MXene Materials Microstructure, College of Physics and Electronic Engineering, Nanyang Normal University, Nanyang 473061, P. R. China*

Junbao He − *Henan International Joint Laboratory of MXene Materials Microstructure, College of Physics and Electronic Engineering, Nanyang Normal University, Nanyang 473061, P. R. China*

Chunying Pu − *Henan International Joint Laboratory of MXene Materials Microstructure, College of Physics and Electronic Engineering, Nanyang Normal University, Nanyang 473061, P. R. China;* orcid.org/0000-0001-8449-0382

Xiaoyu Huang − *Henan International Joint Laboratory of MXene Materials Microstructure, College of Physics and Electronic Engineering, Nanyang Normal University, Nanyang 473061, P. R. China*

Yichong Chen − *Henan International Joint Laboratory of MXene Materials Microstructure, College of Physics and Electronic Engineering, Nanyang Normal University, Nanyang 473061, P. R. China*

Xiaohong Lu − *Henan International Joint Laboratory of MXene Materials Microstructure, College of Physics and Electronic Engineering, Nanyang Normal University, Nanyang 473061, P. R. China*

Yang Lu − *Key Laboratory of Microelectronics and Energy of Henan Province, Engineering Research Center for MXene Energy Storage Materials of Henan Province, Henan Joint International Research Laboratory of New Energy Storage Technology, Xinyang Normal University, Xinyang 464000, P. R. China;* orcid.org/0000-0003-3380-5916

Deyang Zhang − *Key Laboratory of Microelectronics and Energy of Henan Province, Engineering Research Center for MXene Energy Storage Materials of Henan Province, Henan Joint International Research Laboratory of New Energy Storage Technology, Xinyang Normal University, Xinyang 464000, P. R. China*

Zhaorui Wang − *Key Laboratory of Microelectronics and Energy of Henan Province, Engineering Research Center for MXene Energy Storage Materials of Henan Province, Henan Joint International Research Laboratory of New Energy Storage Technology, Xinyang Normal University, Xinyang 464000, P. R. China*

Paul K. Chu − *Department of Physics, Department of Materials Science & Engineering, and Department of Biomedical Engineering, City University of Hong Kong, Kowloon, Hong Kong, China;* orcid.org/0000-0002-5581-4883

Complete contact information is available at:
https://pubs.acs.org/10.1021/acsomega.3c06674

Notes

The authors declare no competing financial interest.

■ REFERENCES

(1) Zhu, X.; Wu, Y.; Lu, Y.; Sun, Y.; Wu, Q.; Pang, Y.; Shen, Z.; Chen, H. Aluminum-doping-based method for the improvement of the cycle life of cobalt-nickel hydroxides for nickel-zinc batteries. *J. Colloid Interface Sci.* **2021**, *587*, 693−702.

(2) Liu, W.; Zhu, F.; Liu, Y.; Shi, W. Hierarchical CoP@Ni(OH)$_2$.0.75H$_2$O core-shell nanosheet arrays on carbon cloth for high-performance supercapacitors. *J. Colloid Interface Sci.* **2020**, *578*, 1−9.

(3) Zhu, M.; Huang, Y.; Deng, Q.; Zhou, J.; Pei, Z.; Xue, Q.; Huang, Y.; Wang, Z.; Li, H.; Huang, Q.; Zhi, C. Highly Flexible, Freestanding Supercapacitor Electrode with Enhanced Performance Obtained by Hybridizing Polypyrrole Chains with MXene. *Adv. Energy Mater.* **2016**, *6*, No. 1600969.

(4) Hwang, H.; Byun, S.; Yuk, S.; Kim, S.; Song, S. H.; Lee, D. High-rate electrospun Ti$_3$C$_2$T$_x$ MXene/carbon nanofiber electrodes for flexible supercapacitors. *Appl. Surf. Sci.* **2021**, *556*, No. 149710.

(5) Wu, Y.; Chen, H.; Lu, Y.; Yang, J.; Zhu, X.; Zheng, Y.; Lou, G.; Wu, Y.; Wu, Q.; Shen, Z.; Pan, Z. Rational design of cobalt-nickel double hydroxides for flexible asymmetric supercapacitor with improved electrochemical performance. *J. Colloid Interface Sci.* **2021**, *581*, 455−464.

(6) Zhou, H.; Wu, F.; Fang, L.; Hu, J.; Luo, H.; Guan, T.; Hu, B.; Zhou, M. Layered NiFe-LDH/MXene nanocomposite electrode for high-performance supercapacitor. *Int. J. Hydrog. Energy* **2020**, *45*, 13080−13089.

(7) Zhang, Y.; Chen, H.; Guan, C.; Wu, Y.; Yang, C.; Shen, Z.; Zou, Q. Energy-Saving Synthesis of MOF-Derived Hierarchical and Hollow Co(VO$_3$)$_2$-Co(OH)$_2$ Composite Leaf Arrays for Supercapacitor Electrode Materials. *ACS Appl. Mater. Interfaces* **2018**, *10*, 18440−18444.

(8) Wang, X.; Yan, C.; Sumboja, A.; Yan, J.; Lee, P. S. Achieving High Rate Performance in Layered Hydroxide Supercapacitor Electrodes. *Adv. Energy Mater.* **2014**, *4*, No. 1301240.

(9) Wang, Q.; O'Hare, D. Recent Advances in the Synthesis and Application of Layered Double Hydroxide (LDH) Nanosheets. *Chem. Rev.* **2012**, *112*, 4124−4155.

(10) Li, K.; Liu, M.; Li, S.; Huang, F.; Wang, L.; Zhang, H. Design on hierarchical P doped Ni(OH)$_2$@Ni-Co LDH core-shell hetero-junction as an advanced battery-like electrode for high performance hybrid supercapacitors. *J. Alloys Compd.* **2020**, *817*, No. 152712.

(11) Chen, H.; Hu, L.; Chen, M.; Yan, Y.; Wu, L. Nickel-Cobalt Layered Double Hydroxide Nanosheets for High-performance Supercapacitor Electrode Materials. *Adv. Funct. Mater.* **2014**, *24*, 934−942.

(12) Zhou, J.-J.; Li, Q.; Chen, C.; Li, Y.-L.; Tao, K.; Han, L. Co$_3$O$_4$@CoNi-LDH core/shell nanosheet arrays for high-performance battery-type supercapacitors. *Chem. Eng. J.* **2018**, *350*, 551−558.

(13) Yang, Q.; Liu, Y.; Xiao, L.; Yan, M.; Bai, H.; Zhu, F.; Lei, Y.; Shi, W. Self-templated transformation of MOFs into layered double hydroxide nanoarrays with selectively formed Co_9S_8 for high-performance asymmetric supercapacitors. *Chem. Eng. J.* 2018, 354, 716−726.

(14) Song, Z.; Meng, Q.; Wei, F.; Yin, Q.; Sui, Y.; Qi, J. In situ hydrolysis strategy to synthesis ultrathin CoNi-LDH nanoflowers for High-performance supercapacitors. *J. Electroanal. Chem.* 2023, 936, No. 117379.

(15) Bai, Z.; Zhang, D.; Guo, Y.; Yang, Y.; Yan, H.; Wang, Y.; Cheng, J.; Chu, P. K.; Pang, H.; Luo, Y. Hierarchical Cobalt-Nickel Double Hydroxide Arrays Assembled on Naturally Sedimented $Ti_3C_2T_x$ for High-Performance Flexible Supercapacitors. *Adv. Sustain. Syst.* 2022, 6, No. 2100371.

(16) Pathak, I.; Acharya, D.; Chhetri, K.; Chandra Lohani, P.; Subedi, S.; Muthurasu, A.; Kim, T.; Ko, T. H.; Dahal, B.; Kim, H. Y. $Ti_3C_2T_x$ MXene embedded metal-organic framework-based porous electrospun carbon nanofibers as a freestanding electrode for supercapacitors. *J. Mater. Chem. A* 2023, 11, 5001−5014.

(17) Li, D.-D.; Yuan, Q.; Huang, L.-Z.; Zhang, W.; Guo, W.-Y.; Ma, M.-G. Preparation of Flexible N-Doped Carbon Nanotube/MXene/ PAN Nanocomposite Films with Improved Electrochemical Properties. *Ind. Eng. Chem. Res.* 2021, 60, 15352−15363.

(18) Zhang, R.; Dong, J.; Zhang, W.; Ma, L.; Jiang, Z.; Wang, J.; Huang, Y. Synergistically coupling of 3D FeNi-LDH arrays with $Ti_3C_2T_x$-MXene nanosheets toward superior symmetric supercapacitor. *Nano Energy* 2022, 91, No. 106633.

(19) Wang, W.; Jiang, D.; Chen, X.; Xie, K.; Jiang, Y.; Wang, Y. A sandwich-like nano-micro LDH-MXene-LDH for high-performance supercapacitors. *Appl. Surf. Sci.* 2020, 515, No. 145982.

(20) Pathak, I.; Acharya, D.; Chhetri, K.; Chandra Lohani, P.; Hoon Ko, T.; Muthurasu, A.; Subedi, S.; Kim, T.; Saidin, S.; Dahal, B.; Yong Kim, H. $Ti_3C_2T_x$ MXene integrated hollow carbon nanofibers with polypyrrole layers for MOF-derived freestanding electrodes of flexible asymmetric supercapacitors. *Chem. Eng. J.* 2023, 469, No. 143388.

(21) Jiang, T.; Wang, Y.; Chen, G. Z. Electrochemistry of Titanium Carbide MXenes in Supercapacitor. *Small Methods* 2023, 7, No. 2201724.

(22) Xie, X.; Zhao, M.-Q.; Anasori, B.; Maleski, K.; Ren, C. E.; Li, J.; Byles, B. W.; Pomerantseva, E.; Wang, G.; Gogotsi, Y. Porous heterostructured MXene/carbon nanotube composite paper with high volumetric capacity for sodium-based energy storage devices. *Nano Energy* 2016, 26, 513−523.

(23) Yan, J.; Ren, C. E.; Maleski, K.; Hatter, C. B.; Anasori, B.; Urbankowski, P.; Sarycheva, A.; Gogotsi, Y. Flexible MXene/ Graphene Films for Ultrafast Supercapacitors with Outstanding Volumetric Capacitance. *Adv. Funct. Mater.* 2017, 27, No. 1701264.

(24) Guo, J.; Zhao, Y.; Jiang, N.; Liu, A.; Gao, L.; Li, Y.; Wang, H.; Ma, T. One-pot synthesis of 2D $Ti_3C_2/Ni_2CO_3(OH)_2$ composite as electrode material with superior capacity and high stability for hybrid supercapacitor. *Electrochim. Acta* 2018, 292, 168−179.

(25) Niu, H.; Yang, X.; Wang, Q.; Jing, X.; Cheng, K.; Zhu, K.; Ye, K.; Wang, G.; Cao, D.; Yan, J. Electrostatic self-assembly of MXene and edge-rich CoAl layered double hydroxide on molecular-scale with superhigh volumetric performances. *J. Energy Chem.* 2020, 46, 105−113.

(26) Shen, J.; Yang, G.; Duan, G.; Guo, X.; Li, L.; Cao, B. NiFe-LDH/MXene nano-array hybrid architecture for exceptional capacitive lithium storage. *Dalton Trans.* 2022, 51, 18462−18472.

(27) Naguib, M.; Kurtoglu, M.; Presser, V.; Lu, J.; Niu, J.; Heon, M.; Hultman, L.; Gogotsi, Y.; Barsoum, M. W. Two-dimensional nanocrystals produced by exfoliation of Ti_3AlC_2. *Adv. Mater.* 2011, 23, 4248−4253.

(28) Edie, D. D. The effect of processing on the structure and properties of carbon fibers. *Carbon* 1998, 36, 345−362.

(29) Fitzer, E.; Frohs, W.; Heine, M. Optimization of stabilization and carbonization treatment of PAN fibres and structural characterization of the resulting carbon fibres. *Carbon* 1986, 24, 387−395.

(30) Zhao, J.; Wang, L.; He, X.; Wan, C.; Jiang, C. A Si-SnSb/ pyrolytic PAN composite anode for lithium-ion batteries. *Electrochim. Acta* 2008, 53, 7048−7053.

(31) Guo, Y.; Zhang, D.; Yang, Y.; Wang, Y.; Bai, Z.; Chu, P. K.; Luo, Y. MXene-encapsulated hollow Fe_3O_4 nanochains embedded in N-doped carbon nanofibers with dual electronic pathways as flexible anodes for high-performance Li-ion batteries. *Nanoscale* 2021, 13, 4624−4633.

(32) Chen, H.; Shen, Z.; Pan, Z.; Kou, Z.; Liu, X.; Zhang, H.; Gu, Q.; Guan, C.; Wang, J. Hierarchical Micro-Nano Sheet Arrays of Nickel-Cobalt Double Hydroxides for High-Rate Ni-Zn Batteries. *Adv. Sci.* 2019, 6, No. 1802002.

(33) Kshetri, T.; Khumujam, D. D.; Singh, T. I.; Lee, Y. S.; Kim, N. H.; Lee, J. H. Co-MOF@MXene-carbon nanofiber-based freestanding electrodes for a flexible and wearable quasi-solid-state supercapacitor. *Chem. Eng. J.* 2022, 437, No. 135338.

(34) Levitt, A. S.; Alhabeb, M.; Hatter, C. B.; Sarycheva, A.; Dion, G.; Gogotsi, Y. Electrospun MXene/carbon nanofibers as supercapacitor electrodes. *J. Mater. Chem. A* 2019, 7, 269−277.

(35) Liu, X.; Zhang, L.; Gao, X.; Guan, C.; Hu, Y.; Wang, J. Enlarged Interlayer Spacing in Cobalt-Manganese Layered Double Hydroxide Guiding Transformation to Layered Structure for High Supercapacitance. *ACS Appl. Mater. Interfaces* 2019, 11, 23236−23243.

(36) Pang, Y.; Li, L.; Wang, Y.; Zhu, X.; Ge, J.; Tang, H.; Zheng, Y.; Wang, F.; Wu, S.; Wu, Q.; Shen, Z.; Chen, H. Zinc-induced phase reconstruction of cobalt-nickel double hydroxide cathodes for high-stability and high-rate nickel-zinc batteries. *Chem. Eng. J.* 2022, 436, No. 135202.

(37) Shahsavari, M.; Mortazavi, M.; Tajik, S.; Sheikhshoaie, I.; Beitollahi, H. Synthesis and Characterization of GO/ZIF-67 Nanocomposite: Investigation of Catalytic Activity for the Determination of Epinine in the Presence of Dobutamine. *Micromachines* 2022, 13, 88.

(38) Ghafoor, M.; Khan, Z. U.; Nawaz, M. H.; Akhtar, N.; Rahim, A.; Riaz, S. In-situ synthesized ZIF-67 graphene oxide (ZIF-67/GO) nanocomposite for efficient individual and simultaneous detection of heavy metal ions. *Environ. Monit. Assess.* 2023, 195, 423.

(39) Wang, S.; Zhang, X.; Xiang, Q.; Zhou, S.; Zheng, J.; Yan, R.; Gao, G. Recyclable non-metal surface-enhanced Raman scattering substrate based on graphene oxide/ZIF-67 nanocomposites. *New J. Chem.* 2023, 47, 13297−13302.

(40) Tang, J.; Jiang, S.; Liu, Y.; Zheng, S.; Bai, L.; Guo, J.; Wang, J. Electrochemical determination of dopamine and uric acid using a glassy carbon electrode modified with a composite consisting of a Co(II)-based metalorganic framework (ZIF-67) and graphene oxide. *Microchim. Acta* 2018, 185, 486.

(41) Lin, K.-Y. A.; Lee, W.-D. Self-assembled magnetic graphene supported ZIF-67 as a recoverable and efficient adsorbent for benzotriazole. *Chem. Eng. J.* 2016, 284, 1017−1027.

(42) Liu, L.; Hu, Z.; Wang, M.; Ma, J.; Chen, Z.; Ning, X.; Yuan, D. Ultrathin NiFe-LDH nanosheets strongly coupled with MOFs-derived hybrid carbon nanoflake arrays as a self-supporting bifunctional electrocatalyst for flexible solid Zn-air batteries. *J. Alloys Compd.* 2022, 925, No. 166665.

(43) Zhao, P.; Fu, S.; Luo, Y.; Peng, C.; Cheng, L.; Jiao, Z. Deciphering the Space Charge Effect of the CoNiLDH/FeOOH n-n Heterojunction for Efficient Electrocatalytic Oxygen Evolution. *Small* 2023, DOI: 10.1002/smll.202305241.

(44) Zhang, T.; Meng, Y.-L.; Zhao, Y.-H.; Ni, J.-C.; Pan, Y.; Dai, Y.; Tan, Z.; Wang, X.-F.; Song, X.-Z. Boosting the oxygen evolution electrocatalysis of high-entropy hydroxides by high-valence nickel species regulation. *Chem. Commun.* 2022, 58, 7682−7685.

(45) Wang, W.; Lu, Y.; Zhao, M.; Luo, R.; Yang, Y.; Peng, T.; Yan, H.; Liu, X.; Luo, Y. Controllable Tuning of Cobalt Nickel-Layered Double Hydroxide Arrays as Multifunctional Electrodes for Flexible Supercapattery Device and Oxygen Evolution Reaction. *ACS Nano* 2019, 13, 12206−12218.

(46) Chen, F.; Chen, C.; Hu, Q.; Xiang, B.; Song, T.; Zou, X.; Li, W.; Xiong, B.; Deng, M. Synthesis of CuO@CoNi LDH on Cu foam

for high-performance supercapacitors. *Chem. Eng. J.* **2020**, *401*, No. 126145.

(47) Guo, J.; Bian, Z.; Ye, L.; Shang, Y.; Guo, F.; Zhang, Y.; Xu, J. Double layers combined with MXene and in situ grown NiAl-LDH arrays on nickel foam for enhanced asymmetric supercapacitors. *Ionics* **2022**, *28*, 2967−2977.

(48) He, M.; He, Y.; Zhou, X.; Hu, Q.; Ding, S.; Zheng, Q.; Lin, D.; Wei, X. Rational design of flower-like Co-Zn LDH@Co(H_2PO_4)$_2$ heterojunctions as advanced electrode materials for supercapacitors. *Dalton Trans.* **2021**, *50*, 4643−4650.

(49) Huang, M.; Wang, Y.; Chen, J.; He, D.; He, J.; Wang, Y. Biomimetic design of NiCo LDH composites linked by carbon nanotubes with plant conduction tissues characteristic for hybrid supercapacitors. *Electrochim. Acta* **2021**, *381*, No. 138289.

(50) Huang, W.; Zhang, A.; Li, X.; Tian, J.; Yue, L.; Cui, L.; Zheng, R.; Wei, D.; Liu, J. Multilayer NiMn layered double hydroxide nanosheets covered porous Co_3O_4 nanowire arrays with hierarchical structure for high-performance supercapacitors. *J. Power Sources* **2019**, *440*, No. 227123.

(51) Xie, L.; Chen, S.; Hu, Y.; Lan, Y.; Li, X.; Deng, Q.; Wang, J.; Zeng, Z.; Deng, S. Construction of phosphatized cobalt nickel-LDH nanosheet arrays as binder-free electrode for high-performance battery-like supercapacitor device. *J. Alloys Compd.* **2021**, *858*, No. 157652.

(52) Wang, P.; Li, Y.; Li, S.; Liao, X.; Sun, S. Water-promoted zeolitic imidazolate framework-67 transformation to Ni-Co layered double hydroxide hollow microsphere for supercapacitor electrode material. *J. Mater. Sci. Mater. Electron.* **2017**, *28*, 9221−9227.

(53) Wang, S.; Huang, Z.; Li, R.; Zheng, X.; Lu, F.; He, T. Template-assisted synthesis of NiP@CoAl-LDH nanotube arrays with superior electrochemical performance for supercapacitors. *Electrochim. Acta* **2016**, *204*, 160−168.

(54) Wang, X.; Sumboja, A.; Lin, M.; Yan, J.; Lee, P. S. Enhancing electrochemical reaction sites in nickel-cobalt layered double hydroxides on zinc tin oxide nanowires: a hybrid material for an asymmetric supercapacitor device. *Nanoscale* **2012**, *4*, 7266−7272.